International Journal of Fatigue 167 (2023) 107343

Contents lists available at ScienceDirect

International Journal of Fatigue

journal homepage: www.elsevier.com/locate/ijfatigue

Ti-6Al-4V powder reuse in laser powder bed fusion (L-PBF): The effect on porosity, microstructure, and mechanical behavior

Arash Soltani-Tehrani [a,b], John P. Isaac [b], Hareesh V. Tippur [a,b], Daniel F. Silva [a,c], Shuai Shao [a,b], Nima Shamsaei [a,b,*]

[a] National Center for Additive Manufacturing Excellence (NCAME), Auburn University, Auburn, AL 36849, USA
[b] Department of Mechanical Engineering, Auburn University, Auburn, AL 36849, USA
[c] Department of Industrial and Systems Engineering, Auburn University, Auburn, AL 36849, USA

ARTICLE INFO

Keywords:
Laser powder bed fusion (L-PBF/LB-PBF)
Additive manufacturing (AM)
Fatigue
Fracture
Part location

ABSTRACT

This work investigated the effects of powder reuse, and location dependency on the mechanical properties of plasma atomized Ti-6Al-4V Grade 5 parts manufactured via laser powder bed fusion (L-PBF). Reusing the powder enhanced powder flowability and packing state while increasing the oxygen. Fatigue performance improved with limited reuse for the specimens upstream of the shield gas and decreased at downstream locations due to large critical defects. Powder reuse increased tensile strength and the critical energy release rate under high strain-rate loading. The specimens in downstream locations suffered more from spattering, resulting in lower fatigue performance and tensile ductility.

1. Introduction

In powder bed fusion (PBF) additive manufacturing (AM) technologies, functional parts can be fabricated from the powder feedstock. Due to the use of powder beds in such technologies and the fact that the fabricated parts only occupy a small fraction (typically < 25 %) of the bed volume, a significant amount of used powder can remain after fabrication. In the applications where the use of unused (i.e., virgin) powder is not mandatory, it is economically appealing to reuse/recycle the used powder for subsequent fabrications to reduce the costs associated with new powder purchase and handling. However, the characteristics of used powders may be significantly different from their unused counterparts which can influence the defect-/micro-structure and result in inconsistencies in the mechanical properties of the fabricated parts.

Careful evaluation of the effect of powder reuse on the powder feedstock-defect-/micro-structure-part performance relationships thus becomes crucial [1]. In fact, America Makes and the American National Standards Institute (ANSI) have listed powder reuse as one of the main AM technical gaps in their Standardization Roadmap for AM [2]. As such, some studies have already attempted to pave the way toward a thorough understanding of the effects of powder reuse on powder characteristics and mechanical properties of AM parts manufactured via electron powder bed fusion (E-PBF) with Ti-6Al-4V (Ti64) [3–8], Inconel 718 (IN718) [9], and Ta [10] powders as well as laser powder bed fusion (L-PBF) with Ti64 [11–16], steels [17–23], IN718 [24–27], AlSi10Mg [28–30], and Hastelloy X [31] powders. However, understanding regarding the powder reuse effect on parts' mechanical properties, especially fatigue, and their location dependency is still lacking, as detailed in the forthcoming text.

During AM process fabrication, powder particles near the parts experience exceeding temperatures [32]. Among them, the smaller ones tend to either melt or be attached to larger particles (forming agglomerates) which are then removed during sieving. Accordingly, the fraction of small particles in a powder batch tends to decrease with limited reuse, and narrow the span of particle size distribution (PSD) [3,6,11,17], typically improving the flowability and powder bed packing state [3,6,11,17,18,24], which can result in less defects in the fabricated parts. However, smaller agglomerates (especially the partially melted

Abbreviations: AE, aeration energy; AM, additive manufacturing/additively manufactured; BFE, basic flowability energy; BDtap, tapped density; CBD, conditioned bulk density; CPS, compressibility; DIC, digital image correlation; E-PBF, electron powder bed fusion; ECCI, electron channeling contrast imaging; EDS, energy-dispersive X-ray spectroscopy; FE, finite element; HCF, high-cycle fatigue; HA, heat-affected; L-PBF, laser powder bed fusion; LCF, low-cycle fatigue; MCF, mid-cycle fatigue; NHT, non-heat-treated; PBF, powder bed fusion; PD, pressure drop; PSD, particle size distribution; SEM, scanning electron microscope/microscopy; SE, specific energy; Ti64, Ti-6Al-4V; UTS, ultimate tensile strength; YS, yield strength.

* Corresponding author at: Department of Mechanical Engineering, Auburn University, Auburn, AL 36849, USA.
E-mail address: shamsaei@auburn.edu (N. Shamsaei).

https://doi.org/10.1016/j.ijfatigue.2022.107343
Received 16 August 2022; Received in revised form 30 September 2022; Accepted 13 October 2022
Available online 19 October 2022

Nomenclature

$2N_f$	number of reversals to failure
ε_f	true fracture strain or ductility
R_σ	the ratio of minimum to maximum stress
S_a	arithmetical mean height of the profiled surface
σ_a	stress amplitude
K_{IC}	fracture toughness
J	energy release rate
J_{IC}	critical energy release rate
east/west specimens	east specimens were closer to the powder feedstock, while the west ones were further away
north/south specimens	north specimens were closer to the gas flow nozzle inlet, while the south ones were in the downstream

ones) can remain even after sieving, and their fraction can increase with reuse. Therefore, the flowability of excessively reused powder is expected to decrease, which can lead to a poorer and more location-dependent powder bed packing state, and, accordingly, higher and more location-dependent defect content in the fabricated parts [17,33]. Although the existence of the non-spherical particles due to powder reuse has been confirmed by several studies [6,10,19,31], to what extent these particles contribute to the aforementioned location-dependency is still not well understood.

In addition to particle morphology, reuse can also increase the O concentration in powder particles [3–6,9–12,20,31]. This again is likely due to the repeated thermal exposure of powder particles near the fabricated parts, which permits the reaction between metal particles and O_2 adsorbed on their surfaces during powder handling [34]. The increased O content in the reused powder may not only lead to a higher concentration of O interstitial atoms in the fabricated parts but also increase the tendency of spattering during fabrication [9,19,20], which can form large defects and nonmetallic inclusions in the fabricated material. The spattering-induced melt pool ejecta (typically oxide-coated metal particles), upon landing back onto the powder bed, can lead to the formation of lack-of-fusion defects due to poor wetting with melts which may increase the O content of the parts in the vicinity [35]. Although shield gas (such as Ar) flow in the build chamber is typically utilized to remove most of the ejecta as they form, some may still land on the powder bed in the downstream locations [33,35]. Therefore, it can be hypothesized that the defect and O contents for parts fabricated at downstream locations are higher, and the upstream–downstream location dependency is expected to increase with reuse. However, the testing of such hypotheses is still lacking in the literature.

The powder reuse-induced variations in the defects contents and microstructure (primarily O concentration) in the fabricated parts can influence their mechanical properties. For instance, higher ultimate tensile strength (UTS) and yield strength (YS) [3,4,6,12,31] and lower tensile ductility [4,7,10,12,19,31] of a wide range of materials, including Ti64 and AlSi10Mg, are typically seen with powder reuse. The higher strengths are generally ascribed to the additional solid solution effect associated with increased O content. The reduced ductility is typically due to the increased defect content, serving as the inception point of fracture [36].

The role of defects is more accentuated in fatigue properties. As a result, the variations in parts' defect content and their location dependency due to powder reuse can translate to relatively large changes in fatigue lives. For instance, an improvement in the high-cycle fatigue performance was observed in Refs. [11,14,17] due to powder reuse, which was associated with a better packing state of reused powder resulting in fewer and smaller defects. Opposite results (i.e., reduction of fatigue performance with reuse) were also reported in Refs. [3,7] due to the formation of lack-of-fusion defects which were ascribed to excessive reduction of fine particles and low aspect ratio (minimum to maximum dimension) powder particles that passed through the sieve. Under high strain-rate loadings, understanding the role of variations from powder reuse induced micro-/defect-structures is still largely lacking, although some data is available for the high strain-rate fracture behavior of some additively manufactured (AM) alloys [37–40] (see Section S4 in the supplemental material for further details).

The current study aims to investigate the effects of powder reuse on mechanical properties, including tensile, fatigue, and high strain-rate fracture behavior of L-PBF Ti64 parts. Any observed variations will be discussed and correlated with powder characteristics, including its flowability, packing state, and chemical composition, as they are affected by powder reuse. In addition, location dependency of mechanical properties with respect to gas flow and powder recoating directions will be investigated. Finally, statistical analysis will be performed to explain the variations in fatigue properties. Following the Introduction, the article will be arranged as follows: Methodology, Experimental Results, Discussion, and Conclusions.

2. Methodology

Plasma atomized Ti64 Grade 5 from the AP&C with a nominal PSD of 15–53 μm was used to fabricate parts using the EOS M290, an L-PBF machine, in an Ar environment employing the EOS recommended process parameters as listed in Table 1. The chemical composition, reported by the manufacturer and measured based on the ASTM F2924 [41], is provided in Table 2.

As seen in Fig. 1, the build layout consisted of 48 larger square bars with a volume of $13 \times 13 \times 100$ mm^3 and 24 smaller square bars with a volume of $9 \times 9 \times 90$ mm^3. The build layout also had 16 net-shaped high strain-rate fracture specimens. A half-built square block was also placed in each quadrant for microstructural analyses. All the coupons located on top of the central line were considered the north group, which was closer to the gas inlet nozzle, and the ones below the line and closer to the gas outlet nozzle were grouped as south. All parts were fabricated on

Table 1
EOS Ti64 Grade 5 HiPer 40 μm process parameters and the calculated energy density.

Parameter Set	Infill	Contour
Laser Power, P (W)	280	240
Scanning Speed, V (mm/s)	1300	900
Hatching Distance, h (μm)	120	(single contour)
Layer Thickness, t (μm)	40	40
Energy Density, E (J/mm^3)*	44.87	–
Power Density, E' (J/mm^2)**	–	6.67

* $E = P/(V \times h \times t)$.
** $E' = P/(V \times t)$.

Table 2
Chemical composition for AP&C plasma atomized Ti64 Grade 5 reported by the manufacturer.

Chemical Composition		
Element	Min (Wt.%)	Max (Wt.%)
Oxygen (O)	–	0.20
Aluminum (Al)	5.50	6.75
Vanadium (V)	3.50	4.50
Iron (Fe)	–	0.30
Carbon (C)	–	0.08
Nitrogen (N)	–	0.05
Hydrogen (H)	–	0.02
Yttrium (Y)	–	0.01
Other elements, each	–	0.10
Other elements, total	–	0.40
Titanium (Ti)	Balance	

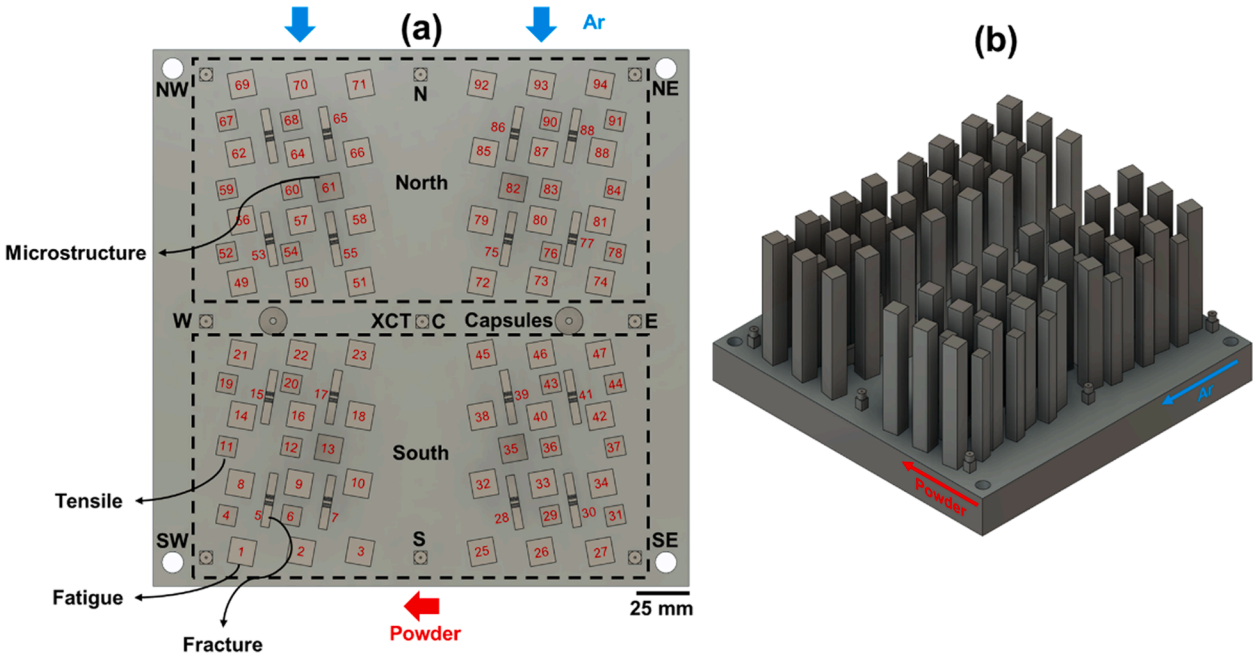

Fig. 1. The (a) top and (b) isometric view of the build layout.

support structures.

Lastly, the build plate contained 9 X-ray computed tomography (XCT) coupons for defect characterization across the build plate (i.e., NW, N, NE, W, C, E, SW, S, and SE) for rapid qualification of the print quality. The build plate density (i.e., defined as the fraction of the build plate area occupied by parts) was 12 % which was well below 25 % recommended by the EOS to prevent the excessive formation of byproducts (e.g., spatter) [42]. The specimen IDs were also labeled on each specimen in Fig. 1. For the reuse strategy, all the powder was collected from the build plate and overflow bin, sieved using an 80-μm filter, and blended with the unused powder remaining from the previous fabrication (see Fig. S1(b) in the Supplemental Material). This process was conducted without adding any unused powder until the remaining powder was not sufficient for subsequent iterations. For each set, ~20 kg of powder was used to cover the whole build plate and fabricate the parts, and ~ 2 kg was consumed for each fabrication without considering the wastes and filtered powder. The initial amount of powder (i.e., 65 kg) was adequate to fabricate 8 times. Each fabrication was ~ 100 hrs of exposure (i.e., a total of 800 hrs) which is among the highest exposure hours in the literature [43].

After fabrication, the XCT and microstructure coupons were removed from the build plate in the non-heat-treated (NHT) condition. The remaining were stress-relieved (SR) at 704 °C for 1 h, followed by furnace cooling in Ar. After SR, the parts were removed from the build plate. The large and small square bars were machined to the geometry of fatigue, and tensile specimens, based on ASTM E466 and E8M [44,45], respectively, as shown in Fig. 2. This figure also shows the geometry of high strain-rate fracture specimens and XCT coupons.

After machining, tension tests were conducted in displacement control mode using an MTS Landmark load frame with 100 kN load cells without further polishing. The strain-rate was kept constant at 0.001 mm/mm/s based on ASTM E8M [45]. An extensometer was used to record the strain, and it was removed post yielding at 0.05 mm/mm. High strain-rate fracture tests were performed using a Kolsky bar apparatus with a striker velocity of ~ 40 m/s. The Digital Image Correlation (DIC) method coupled with ultrahigh-speed photography was employed to obtain time-resolved in-plane deformations on the specimen surface. A Kirana-05 M camera (924 × 768 pixels) fitted with an 80–400 mm focal length lens and adjustable bellows was used to record speckle images at a rate of 400,000 frames per second.

The experimentally measured displacements from DIC were exported into Finite Element (FE) nodes as boundary conditions to evaluate the fracture properties of interest, namely the *J*-integral [40,46] (further details are provided in Section S4 in the Supplemental Material). Fully-reversed fatigue tests ($R_\sigma = -1$) were run via the MTS Landmark and MTS Bionix Tabletop load frames. The force-controlled tests were conducted at 400, 500, 600, and 700 MPa stress levels with 6, 5, 4, and 3 Hz frequencies, respectively, to probe fatigue behavior in the mid-cycle and high-cycle fatigue regimes (MCF and HCF) based on ASTM E466 [44]. The different frequencies were used to ensure approximately the same cyclic strain rates at all stress levels. Failure was defined as the complete fracture of each specimen, and tests that did not fail before 5×10^6 cycles (i.e., 10^7 reversals) were considered run-out.

Using a Zeiss Crossbeam 550 scanning electron microscope (SEM), all fracture surfaces and the microstructure of Ti64 specimens were investigated. The crack-initiating defect sizes were evaluated with the FIJI software [47]. The chemical composition on the fracture surfaces near the defects was also obtained by the Oxford energy-dispersive X-ray spectroscopy (EDS) instrument. The microstructure in the NHT condition was also investigated for all prints via electron channeling contrast imaging (ECCI) using the SEM. The images were obtained from the longitudinal plane (i.e., along the building direction). A Zeiss Xradia 620 Versa was utilized for XCT scans to examine the defect content within the specimens using a source voltage of 140 kV, power of 21 W, and a voxel size of 5 μm. The 3D visualizations and defect distributions were obtained via Dragonfly Pro and FIJI, respectively.

Before each fabrication, the powder was sampled according to ASTM B215 [48] from the feedstock bin. Some heat-affected (HA) powder with particles ejected from the melt pools and near the gas flow outlet nozzle (see Fig. S1(a) in the Supplemental Material) were also collected for further investigations. All powder PSDs were analyzed using a Beckman Coulter LS 13 320 Particle Size Analyzer using the laser diffraction method. The concentration of interstitial elements (including O and N) in powder batches was analyzed using LECO 736 Series Inert Gas Fusion according to ASTM E1409 [49]. Powder rheological characteristics were measured via an FT4 powder rheometer according to ASTM D7891 [50] and the FT4 manual [51]. Powder characteristic measurements were repeated four times to ensure repeatability.

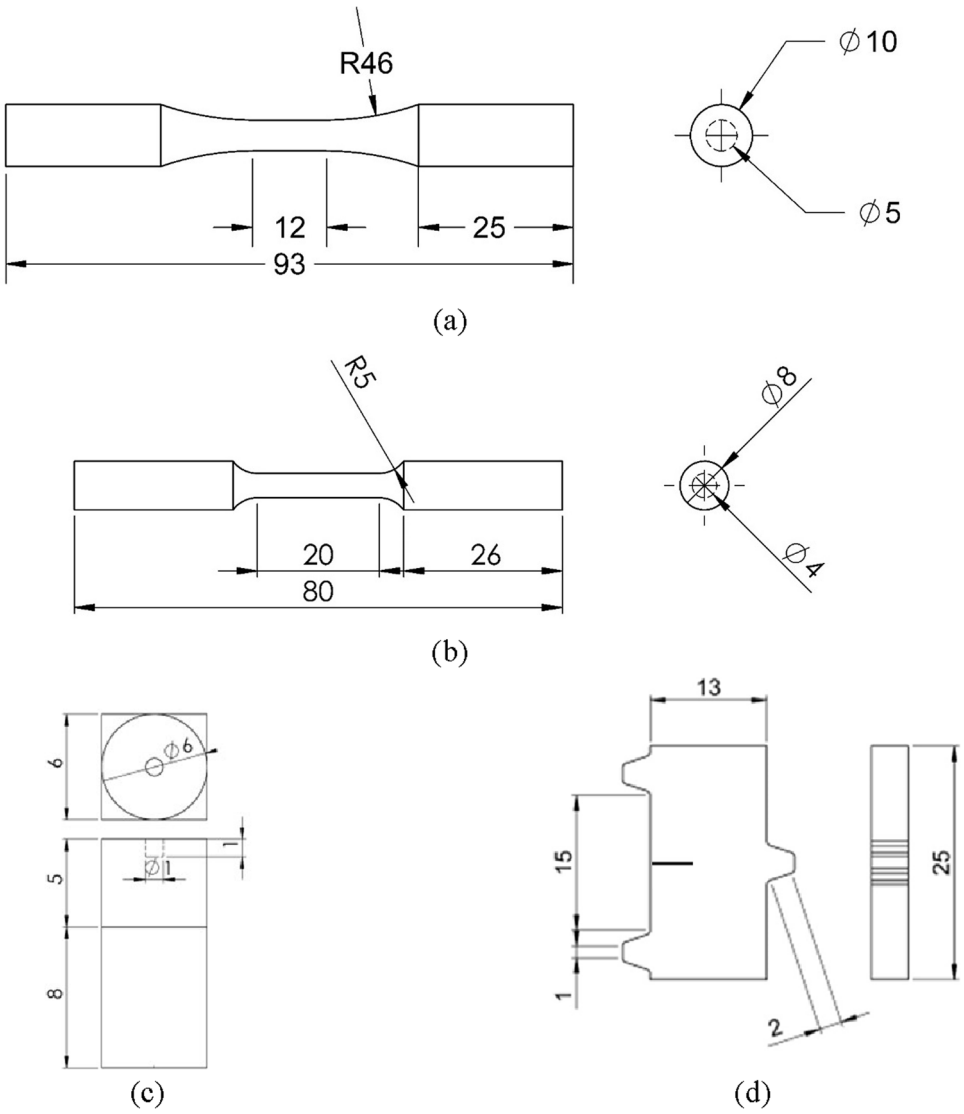

Fig. 2. The geometries of (a) round fatigue specimens with 5-mm straight gage diameter according to ASTM E466 [44], (b) round tension test specimen with 4-mm straight gauge diameter according to ASTM E8M [45], (c) XCT coupon, and (d) high strain-rate fracture specimen. All dimensions are in mm.

3. Experimental results

3.1. Powder characteristics

As seen in Fig. 3(a), the PSDs of the feedstock (i.e., the powder used for fabrication) indicated a slight increase in particle size with powder reuse. In addition, the corresponding D_x-values are reported in Fig. 3(c). The D_x indicates that the x% of the particles have an equivalent diameter smaller than the D-value [52,53]. The gradual increase of the D-values can be ascribed to the removal of fine particles, which are easier to melt and be attached to other particles and part surfaces [42,54]. Closer inspection of the PSDs showed a secondary peak in PSD of Print 8 powder between 80 and 100 μm. This peak corresponded to ~ 1 % of the total population of Print 8 powder particles. This observation was quite interesting as the sieve used for filtering the particles had a nominal size of 80 μm. Therefore, it may be that some of these particles had low aspect ratios (the ratio of minimum to maximum orthogonal dimensions) and passed through the sieve (e.g., elongated particles and agglomerates) [3]. The particle size span (i.e., D_{90}-D_{10}/D_{50} [55]), which characterizes the width of the PSD peak, did not change with the powder reuse (i.e., 0.8 for all batches). The HA powder (i.e., the powder after fabrication and near the gas outlet) PSDs were consistently larger than the feedstock in all prints (see Fig. 3(b)).

The D_{90} value was exceedingly high in the HA powder, which was attributed to the presence of very large particles that were either large, resolidified melt pool ejecta or large agglomerates of smaller particles due to heat exposure [56–59] (see Fig. 3(a-c)). The HA powder span was twice the powder feedstock (i.e., 1.6), showing a wide range of particle sizes. The particle circularity and aspect ratio were evaluated from the 2D images of the powder with microscopy (see Fig. 4). Some non-spherical elongated particles were observed in Print 8. The aspect ratios of particles 1, 2, and 3 in Print 8 (see Fig. 4(c) & (d)) were 0.5, 0.4, and 0.4, with circularities of 0.7, 0.6, and 0.7, respectively. Such low aspect ratio particles or agglomerates could possibly form due to the collision of melt pool ejecta in the chamber environment [56]. These particles were more frequently seen in the Print 8 powder due to longer exposure to the laser [3]. Such agglomerates could pass through the sieve and, with sufficient quantity, compromise powder spreading and bed packing, potentially resulting in poorer mechanical properties of AM parts [56,60].

The powder feedstock rheological characteristics were evaluated and reported in Table 3. The basic flowability and specific energies can

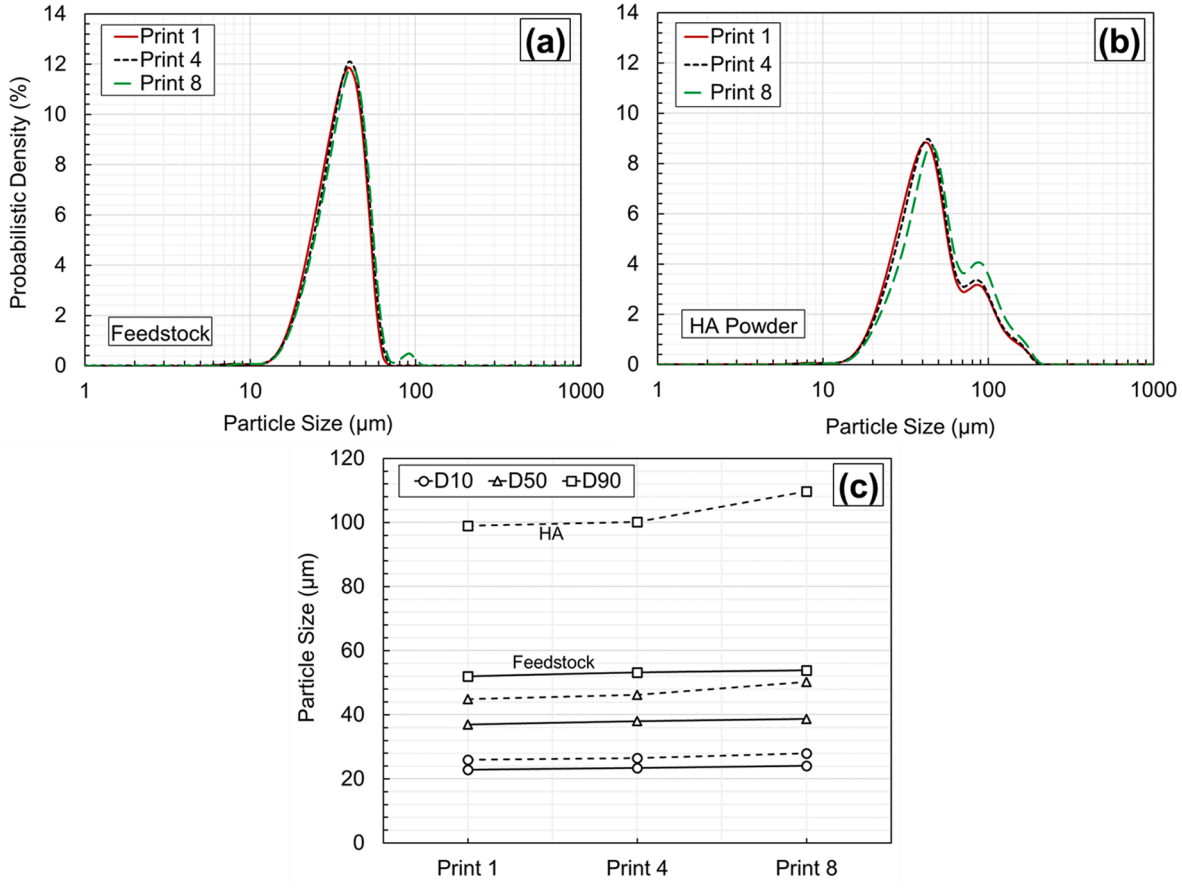

Fig. 3. PSD of the (a) feedstock and (b) HA powder samples, as well as the corresponding D-values of the (c) feedstock and HA powders. The solid and dashed lines correspond to feedstock and HA powders in (c), respectively.

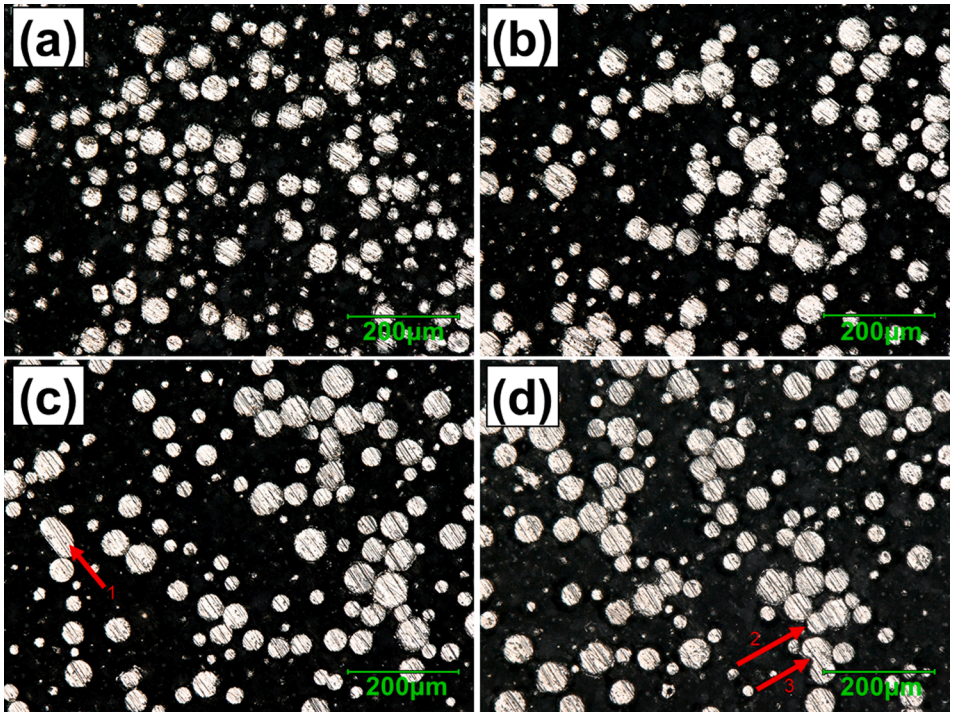

Fig. 4. Polished powder particle cross-sections for Prints 1 in (a), 4 in (b), and 8 in (c) and (d). The red arrows are pointed toward the low aspect ratio particles. (For interpretation of the references to color in this figure legend, the reader is referred to the web version of this article.)

Table 3
A summary of powder rheological and bulk characteristics for Prints 1, 4, and 8.

Powder Characteristic	Print 1 (Unused)	Print 4 (3x-Reused)	Print 8 (7x-Reused)
Basic Flowability Energy, BFE (mJ)	277.75 ± 16.51	289.00 ± 13.06	288.25 ± 8.97
Specific Energy, SE (mJ/g)	1.81 ± 0.11	1.53 ± 0.05	1.56 ± 0.03
Conditioned Bulk Density, CBD (g/mL)	2.73 ± 0.01	2.75 ± 0.01	2.76 ± 0.01
Tapped Density, BDtap (g/mL)	2.83 ± 0.02	2.83 ± 0.01	2.84 ± 0.01
Compressibility, CPS (%)	2.85 ± 0.23	2.37 ± 0.43	2.01 ± 0.24
Cohesion, c (kPa)	0.14 ± 0.01	0.10 ± 0.02	0.09 ± 0.03
Pressure Drop, PD (mBar)	6.60 ± 0.48	6.92 ± 0.54	7.38 ± 0.36
Aeration Energy, AE (mJ)	5.38 ± 0.88	5.44 ± 0.28	5.44 ± 0.44

quantify the powder flowability by measuring the energy required for the blade to move respectively downward or upward within the powder bulk [53,61]. While the basic flowability energy did not exhibit significant change, the specific energy slightly decreased with powder reuse, indicating some improvement in the powder flowability on the powder bed during fabrication [55,62,63]. This flowability improvement with powder reuse was also observed in cohesion values. The cohesion evaluates the powder flow behavior when sheared. Lower cohesion can represent a lower resistance to flow and a more uniform powder bed, yielding less east-to-west location dependency of the parts on the build plate [17,51,53,55,61].

The powder bed packing state improved with powder reuse. This behavior was noted by evaluating the powder compressibility and conditioned bulk density. The former indicates the volume change when the powder is compressed [53], and the latter is measured when the powder bulk is in a low-stress condition (i.e., loosely packed) [53,61]. Therefore, the reducing compressibility and increasing conditioned bulk density at higher print numbers shown in Table 3 indicated the improving packing state of metal powder bed with reuse [11,17,55]. This observation was consistent with the increasing pressure drop values as reuse times increased [51]. A higher pressure drop can indicate a more tightly packed powder bed; i.e., a better packing state [17,53].

As seen in Fig. 5(a), the concentrations of interstitial elements (i.e., O and N) in the powder increased by powder reuse, similar to Ref. [54,62]. The O and N concentrations of the HA powders were also investigated (see Fig. 5(b)). In the HA powder, the concentration of N significantly increased beyond the threshold value with Print 8, whereas the concentration of O did not change significantly and maintained around the threshold value. Therefore, it was deduced that the increase of O and N in the reused feedstock batches was due to the HA particles which passed through the sieve and mixed with the feedstock powder [60,62]. The increase in O and N contents has been ascribed to the exposure of powder to residual gases in the chamber and those adsorbed to the powder surface during powder handling at elevated temperatures during fabrication [64], which intensifies with longer exposure hours. However, the uptake of N in the HA powder was much more drastic than the feedstock material. This may be due to the residual N_2 concentration in the chamber after Ar purging being higher than that of O_2, at a 4:1 ratio [64]. Therefore, although Ti has a higher chemical affinity with O rather than N [65], the hot melt pool ejecta could still react with the residual N_2 easier.

These HA powder particles formed from ejecta were larger (see Fig. 3 (b)) and could be easily filtered out during sieving, which resulted in considerably lower N uptake in the feedstock powder. Although no characterization was conducted on the particles remaining on the sieve, it is nevertheless interesting to investigate the fraction of *N*-rich particles on the sieve in future studies. It is noteworthy that the amounts of O and N in the feedstock powders were still well below the maximum permitted amount per ASTM F2924 [41]. Some studies have associated the increase in elements such as O and N with a decrease in Ti melting temperature and consequently unstable molten flow [66], leading to rougher surfaces and interrupted powder flow [67,68]. In this regard, higher surface roughness was generally observed for the specimens manufactured from the reused powder regardless of the location, which was consistent with the PSD and chemical composition changes (see Fig. S2 in the Supplemental Material). Although this work focused mostly on the tensile and fatigue properties measured from surface machined specimens, care must be taken if the specimens are tested in their as-built surface condition due to the detrimental effects of surface micro-notches [69,70].

3.2. Defect content and microstructure

The XCT witness coupons were used to track any discernible trends of build quality with respect to powder reuse and location on the build plate. Defects smaller than four times voxel size (i.e., 20 μm) were removed to avoid false detection from noise. Upon XCT characterization, some high-density pixels were also detected. Some studies have correlated these dense pixels with secondary phase particles [71]. Since none of the fatigue failures initiated from such inclusions, they were excluded from the XCT analysis to only characterize the defect content. The results were then clustered in [20, 30), [30, 40), and [40, ∞) μm size

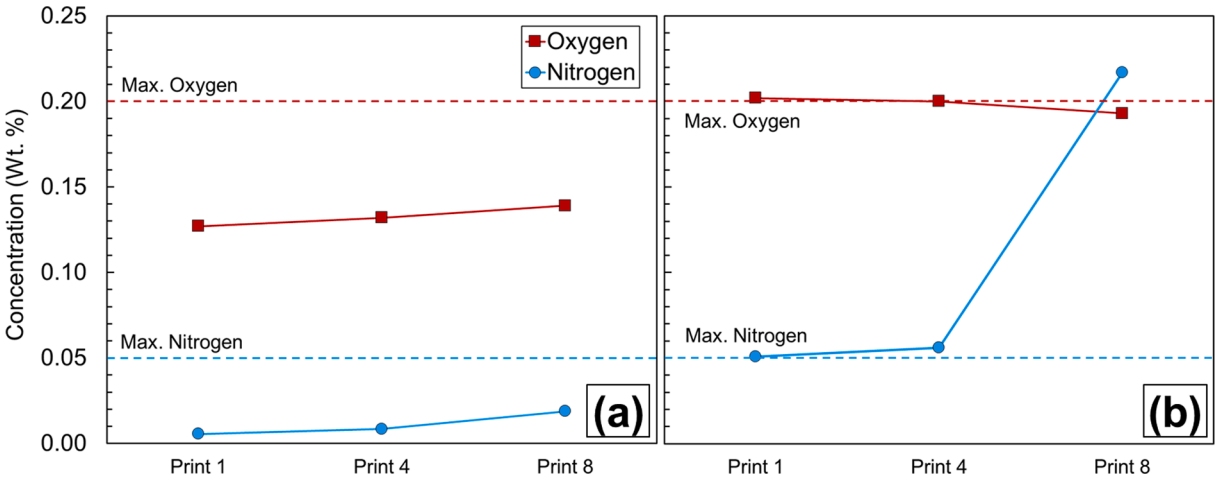

Fig. 5. The concentration of interstitial elements (O and N) in the (a) feedstock and (b) HA powders with respect to powder reuse. The feedstock and HA powders were collected before and after fabrication, respectively.

ranges and reported in Fig. 6.

As seen in Fig. 6, there was generally a decreasing trend in the number and equivalent sphere diameter (i.e., the diameter of a sphere whose volume equals that of the defect's) of the defects by reusing the powder up to Print 4. However, further powder reuse up to Print 8 increased both defect diameter and number compared with Print 4. In addition, no clear trend in defect content was observed in the direction of the powder delivery (i.e., recoater direction), although some minor particle segregation was previously observed (see Fig. 3(d)). However, consistent with the results in Ref. [33], the number of defects increased along the gas flow direction, which may be attributed to melt pool ejecta not being properly removed from the build chamber by the gas flow and landing in such regions. This increase was more apparent for Print 8. The maximum defect size did not show a clear trend with respect to powder spreading direction. Although not significant, it somewhat increased in the gas flow direction, especially for the reused powder.

As seen in the ECCI micrographs shown in Fig. 7, the changes in microstructure with powder reuse were negligible in the NHT condition. In Prints 1, 4, and 8 specimens, the darker phases appeared to be martensitic (i.e., α' and α") due to high cooling rates associated with L-PBF technology [1]. Although the rapid cooling was expected to generate purely martensitic microstructure, the repeated reheating due to the consolidation of the subsequent layers may have partially decomposed the microstructure to α + β. Indeed, the phases with brighter contrast appeared to be β due to the partial decomposition. The grain size was almost comparable for all powders.

3.3. Tensile behavior

Tensile properties, including UTS, YS, and ductility (ε_f) were obtained for all tension test specimens to analyze their location dependency and the effect of reuse. Here, only the north and south locations, i.e., the upstream and downstream locations of the shielding gas flow, were of focus since no general trends in defect content were observed in the powder spreading direction (i.e., east to west). Accordingly, there were six specimens per reuse condition and location (i.e., north and south). The results of the total of 36 tensile tests are presented in Fig. 8. As seen in Fig. 8(a), an increasing trend in UTS was noticeable with powder reuse in both the north and south specimens. The YS also showed the same trend for both the location and the powder

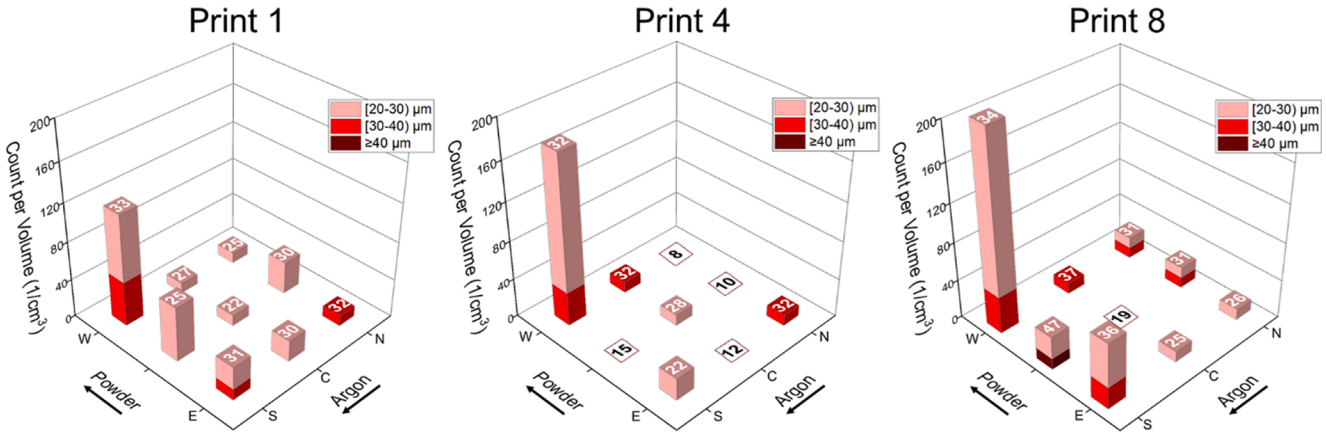

Fig. 6. 3D bar charts indicating defect distributions in the XCT coupons across the build plate with powder reuse and the maximum defect size labeled on each bar. The color-gradient columns consisting of lighter to darker colors represent smaller to larger defect size ranges.

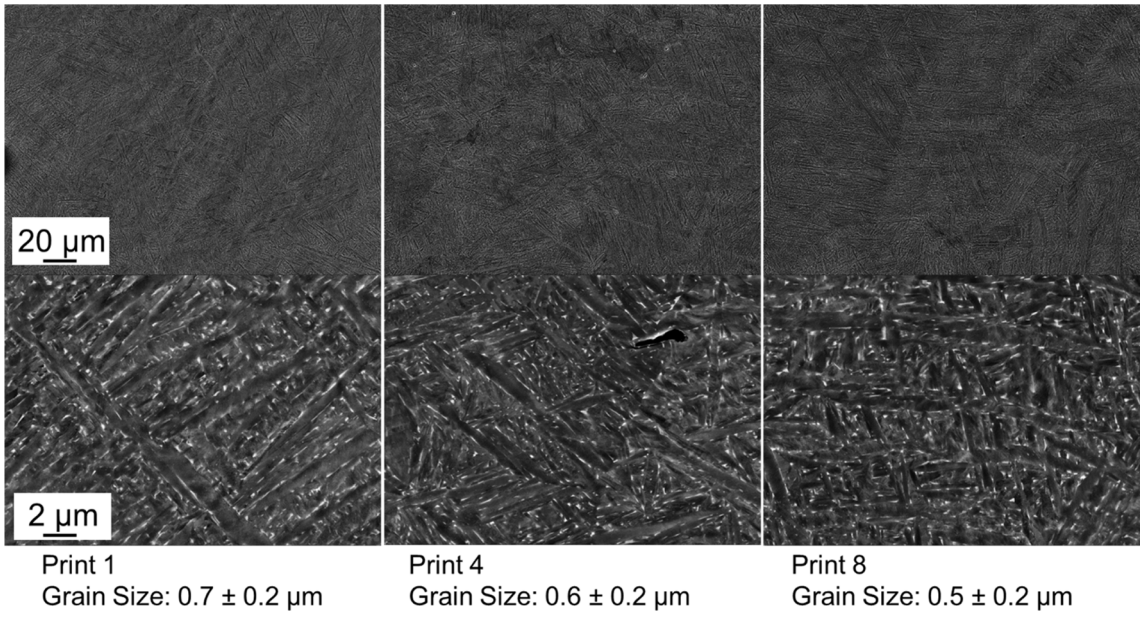

Fig. 7. The microstructure of L-PBF Ti64 in the NHT condition for Prints 1, 4, and 8.

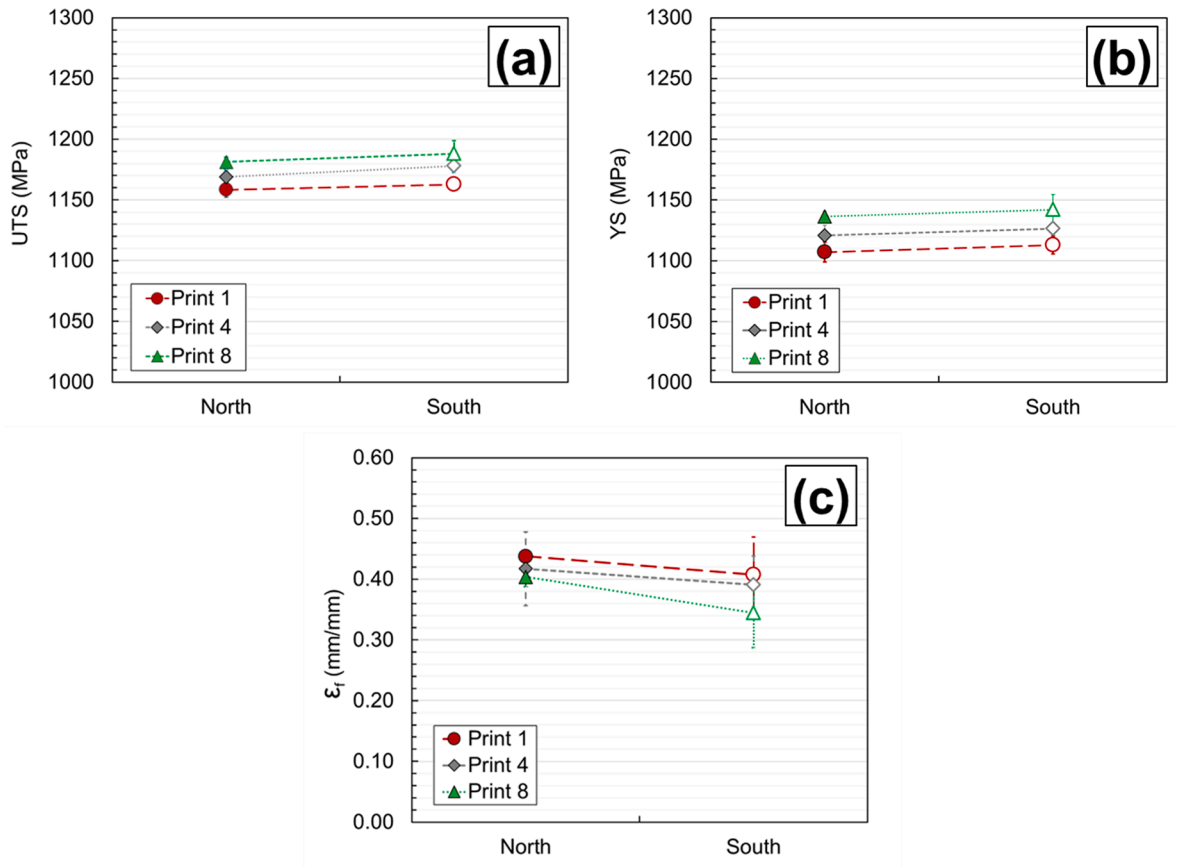

Fig. 8. Tensile properties, including (a) UTS, (b) YS, and (c) ε_f obtained for different prints and locations on the build plate.

reuse (see Fig. 8(b)), which can be due to the low hardening rate of Ti64. Although the relative changes in strength were small, i.e., ~2.5 %, they were evidently beyond the scatter among the 6 tests in each specimen condition (as indicated by error bars). As shown in Fig. 7, the microstructure of fabricated parts was not affected by powder reuse. Therefore, the added strength with reuse was ascribed to some increase in O and N concentrations in the powder (see Fig. 5(a)) and in the specimens, which have both strengthening effects [65,72]. It is generally known that O and N concentrations can increase strength and reduce ductility [16,31,64,73–75]. Such changes in tensile properties have been associated with the role of these solute atoms in twinning and slip restriction [72,74]. In contrast, the influence of location on UTS and YS was considerably less regardless of the powder condition (see both Fig. 8(a) & (b)). Unlike tensile strength, the ε_f somewhat decreased with powder reuse (see Fig. 8(c)). This decrease was more drastic for the specimens in the south. Noting that the defect content was expected to improve at Print 4 (see Fig. 6)—yet the ductility still reduced; thus, the role of O concentration in the powder (see Fig. 5(a)) may have been significant. Nevertheless, the tensile ductility observed in the south locations for Print 8 was substantially lower than all other conditions, which could have been contributed by the relatively high defect content witnessed in the south of Print 8 and the increased O and N contents [76]. Noted that all error bars indicated in Fig. 8 were calculated based on six tensile tests per powder reuse condition and location (i.e., 36 tensile tests in total) using two times standard deviation and represented by full bars. In addition, the corresponding stress–strain diagrams for some of the tensile tests are shown in see Fig. S10 in the Supplemental Material.

3.4. High strain-rate fracture behavior

High strain-rate tests were conducted on high strain-rate fracture specimens following a methodology explained in detail in Section S4 of the Supplemental Material. The *J*-integral or the energy release rate histories for the horizontally built specimens (Loading axis and crack were perpendicular to the build plate) from Prints 1, 4, and 8 (six specimens per condition) are shown in Fig. 9. From the DIC images, crack initiation was identified in each experiment, and that image or dataset was identified as $t = 0$ μs to create a common reference time for comparing all experiments. Therefore, negative and positive time instants represent the response before and after the crack initiation, respectively. It can be noted that the whole fracture event, from initial contact to crack initiation and growth, lasted ~ 60 μs. The data in Fig. 9 (a) corresponds to the specimens from the north in each print. The *J*-integral values overlapped until crack initiation (or time $t \sim 0$ μs), and the variations were approximately parabolic. However, the values showed differences at crack initiation.

The *J*-integral at crack initiation was the highest for specimens from Print 8 at 19.4 kJ/m^2, followed by Print 4 at 19.2 kJ/m^2, and Print 1 at 18.6 kJ/m^2. The crack propagation behaviors had a similar response for all prints. Hence, considering all three, Prints 4 and 8 had 3 % and 4 % higher critical energy release rates than Print 1. The crack growth resistance curves under dynamic loading conditions are shown in Fig. 9 (b). The crack growth was stable, as reflected by the non-negative slope of the resistant curve ($dJ/da \sim 0$) after crack initiation. The slopes after crack initiation also remained the same for all prints with just the difference in magnitude due to the higher critical energy release rate for Prints 4 and 8.

The similarity of fracture behaviors of Ti64 specimens fabricated from different locations on the build plate in Print 1 is shown by the *J*-integral histories in Fig. 10(a) and crack growth resistance curves in Fig. 10(b). As shown, there was no significant difference in the critical energy release rate for the specimens from different locations, i.e., no location dependency. Specifically, a maximum of 2 % difference was observed between the south and north in Print 1. However, the

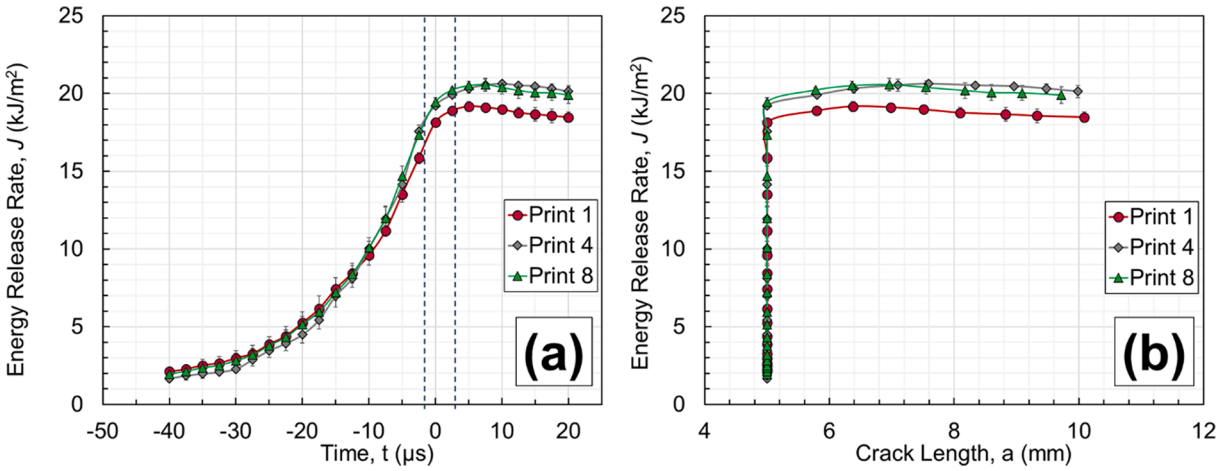

Fig. 9. The *J*-integral histories (a) and crack growth resistance curves (b) for Ti64 specimens from Prints 1, 4, and 8. All data is from the specimens in the north.

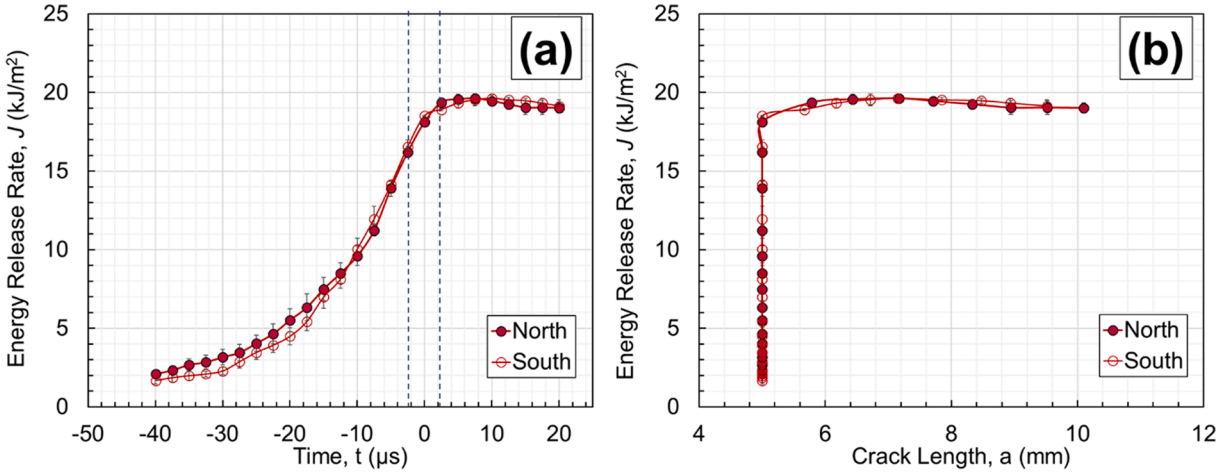

Fig. 10. The *J*-integral history (a) and crack growth resistance curves (b) for Ti64 specimens from Print 1 in the north and south locations of the build plate.

experimental error was also ~ 2 %. Similar behavior was also observed for Prints 4 and 8 (See Figs. S7 and S8 in the Supplemental Material). A summary of high strain-rate fracture results at two different time instants is reported in Fig. 11. In Fig. 11(a), critical energy release rates ($t = 0$ μs) are shown for specimens fabricated in north and south locations, and their values are listed in the table below the figure. It can be observed that the difference in fracture properties because of the location was within the experimental error (~2%). However, a discernible difference was observed between Print 1 and Prints 4 and 8. The difference between Prints 4 and 8 was still within the experimental error. Prints 4 and 8 had a 3 % and 4 % increase in energy release rate at $t = 0$ μs compared to Print 1, respectively. In Fig. 11(b), energy release rates during crack growth at $t = 7.5$ μs are shown for their respective north and south locations. Similar trends of improved critical energy release rate were observed for Prints 4 and 8 when compared to Print 1. As discussed earlier, time $t = 0$ μs was identified as the instant at which cracks initiated on the surface of the specimen that was imaged. However, the crack might not have initiated uniformly over the entire crack front of the specimen at the same time instant due to the finite thickness. Hence, observing the behavior at a later time instant minimizes this ambiguity. At $t = 7.5$ μs, however, Prints 4 and 8 showed a slightly higher, 6 % and 7 %, increase in the energy release rate relative to Print 1, respectively.

3.5. Fatigue behavior & failure analysis

Since defect contents only showed significant variation along the gas flow direction (see Fig. 6), fatigue performance was merely compared between the north and south specimens. Among the specimens located in the north, the ones in Print 4 had somewhat better fatigue performance, followed by Prints 1 and 8 (see Fig. 12). However, in the south, Print 1 outperformed Print 4 and 8. The better fatigue performance for the reused powder in the north agreed with the results in Ref. [11], which might have been due to the better packing state of reused powder (see Table 3). The reduced fatigue performance in the north for Print 8 was perhaps due to the increased spattering activities caused by the increased O and N contents in the powder. South locations were at the downstream of the shielding gas, and the effect of spattering was, therefore, more significant. As a result, reduced performance in the south was seen as early as Print 4. Location dependency of fatigue behavior for specimens from Prints 1, 4, and 8 was characterized and presented in Fig. 13. The specimens fabricated in the south generally had lower fatigue lives irrespective of the powder reuse.

The south-to-north difference was less significant in Print 1. As the powder was reused, the gap became more distinct in Print 4. With continued reuse, the gap appeared to become small again in Print 8. This interesting behavior may be related to changes in defect content within the specimens in the north and south due to powder reuse. As briefly discussed in the Introduction, the increased O and N concentrations in powder with reuse tend to induce more frequent spattering, which can

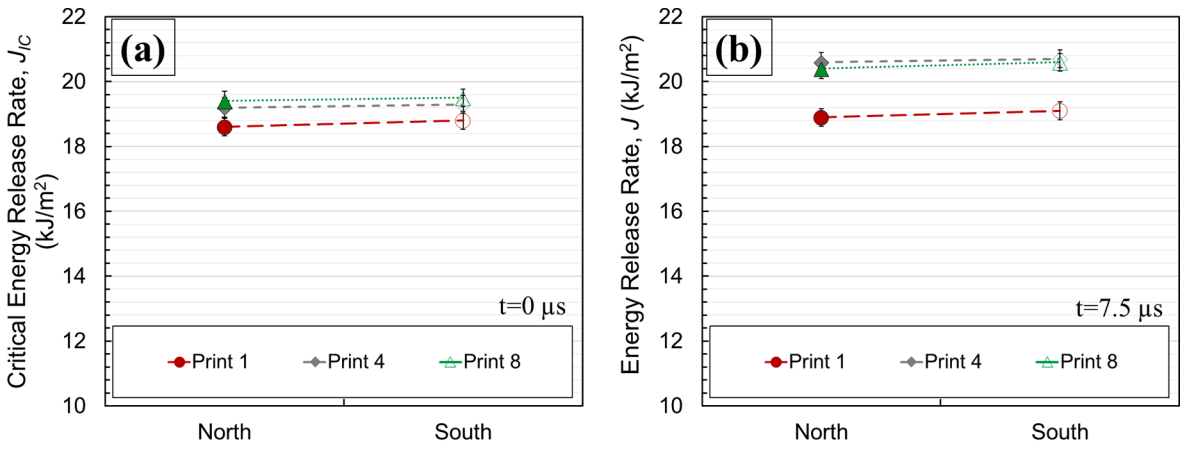

J_{IC} (kJ/m²)	North	South
Print 1	18.6	18.8
Print 4	19.2	19.3
Print 8	19.4	19.5

J (kJ/m²)	North	South
Print 1	19.1	19.2
Print 4	20.4	20.4
Print 8	20.5	20.6

Fig. 11. A summary of the energy release rate for Ti64 specimens for different powders and locations on the build plate at (a) t = 0 µs and (b) t = 7.5 µs.

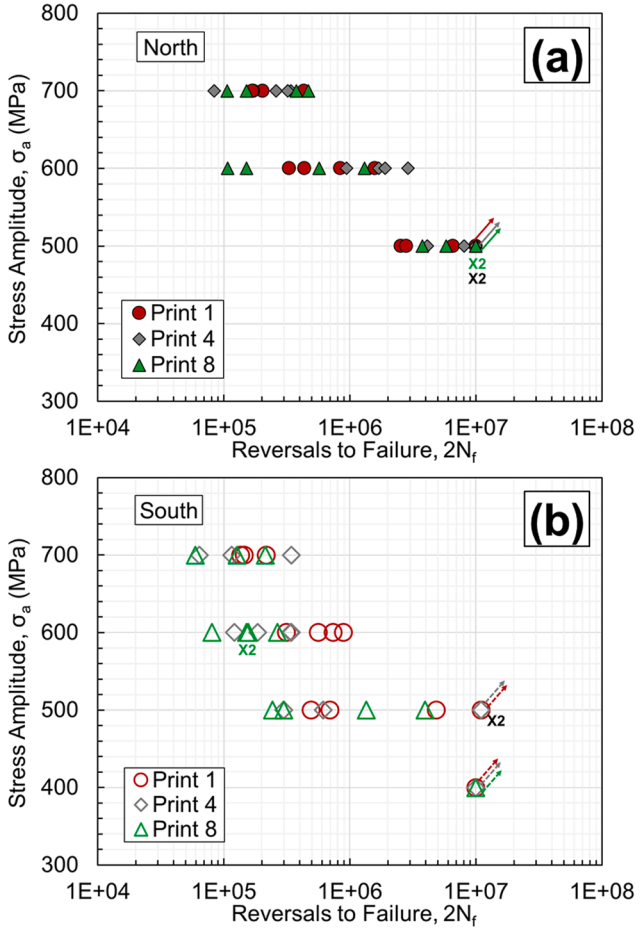

Fig. 12. Stress-life fatigue behavior of L-PBF Ti64 Grade 5 specimens from Prints 1, 4, and 8 in (a) north and (b) south.

form more defects of larger size. Due to the shield gas flow, more pronounced excessive defect formation first occurred at the downstream locations (south), and as O concentration increased, it proliferated gradually to the north. This hypothesis is tested in Section 4 with complete information on critical defects' size.

A summary of all force-controlled fatigue tests is reported in Table 4. Fracture surfaces of all fatigue specimens were examined, and the size and location of the crack initiating defects are also listed in Table 4. In this table, the defect size was measured based on Murakami's $\sqrt{area}$ approach. In this method, defects were classified based on their location from the surface (i.e., internal or at the surface). When the defect is neither internal nor at the surface, i.e., sub-surface, the whole defect and the adjacent area between the defect and surface were considered as the area, provided that its size is larger than the distance to the free surface [77]. A visual illustration of fatigue lives of failed specimens and the corresponding defect size is shown in Fig. S11 in the Supplemental Material. Some notable fracture surfaces are also shown in Fig. 14. One of the specimens of interest was Sp. 1, which was located the closest to the shielding gas outflow nozzle and had lower fatigue life than other specimens at the same stress level. As seen in these figures, all failures initiated from irregular-shaped lack-of-fusion defects, typically larger for the specimens located in the south (i.e., Sp 1 and 27). It was reported that excess O content (e.g., in the form of oxides) could also promote the formation of such lack-of-fusion defects, possibly via spattering, in Ti64 [5].

As evident in Fig. 14 and Table 4, the size of defects increased with reusing the powder for the south specimens compared to Print 1. The equivalent defect size was measured based on Murakami's approach [53,78,79] and found to be 81, 162, and 151 µm, respectively, for Print 1, 4, and 8 specimens. This observation was consistent with the O pickup noted with powder reuse, which could have resulted in more spatter. In addition, due to the higher probability of spatters landing in the south region, the defects in these specimens were somewhat larger (see Table 4). The equivalent defect size in the Print 1-south specimens was 81 and 93 µm, respectively, whereas it was 71 and 81 µm for the case of Print 1-north specimens.

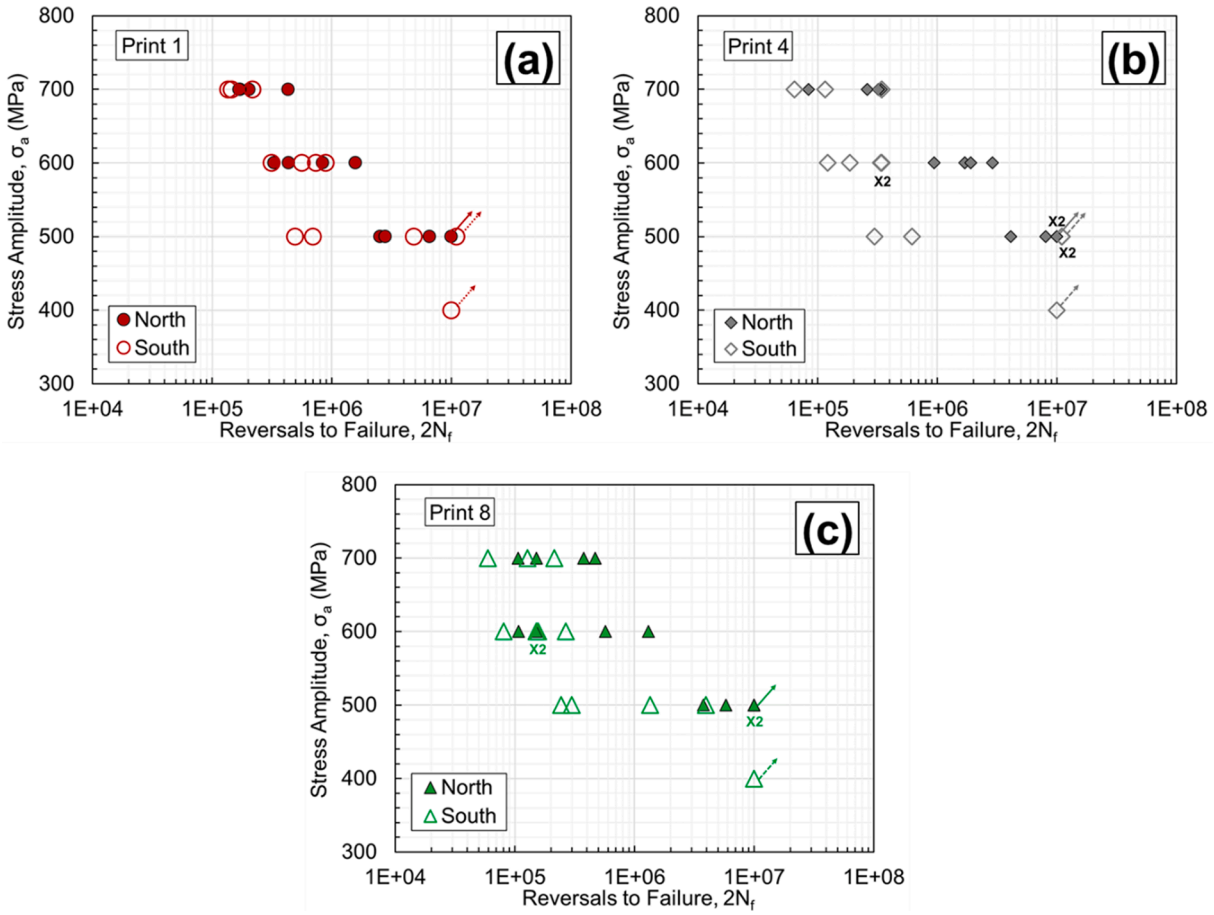

Fig. 13. Stress-life fatigue behavior of L-PBF Ti64 Grade 5 specimens from Prints (a) 1, (b) 4, and (c) 8 in the north and south regions.

Table 4
A summary of fully-reversed (R_σ = -1) force-controlled fatigue tests for L-PBF Ti64 specimens in machined surface conditions for Prints 1, 4, and 8 with the corresponding equivalent defect size and location, including internal (I), surface (S), and sub-surface (SS).

ID	σ_a(MPa)	Print 1		Print 4		Print 8	
		$2N_f$ (Reversals)	Size (μm), Location	$2N_f$ (Reversals)	Size (μm), Location	$2N_f$ (Reversals)	Size (μm), Location
South							
22	400	> 10,000,000		> 10,000,000		> 10,000,000	
01	500	491,454	81, I	299,142	162, I	242,984	151, I
27	500	694,022	93, I	615,804	82, I	297,506	153, I
38	500	4,855,624	34, I	> 10,000,000		1,346,636	102, SS
18	500	> 10,000,000		> 10,000,000		3,937,652	42, I
03	600	314,492	129, I	185,184	105, I	151,290	125, I
42	600	561,396	49, I	338,338	159, I	265,448	171, SS
14	600	737,294	65, SS	120,800	116, SS	155,806	121, I
25	600	886,098	46, I	343,684	108, I	80,364	99, SS
09	700	135,700	79, I	63,978	127, SS	59,608	106, I
33	700	145,022	57, I	115,778	95, I	126,954	69, I
46	700	216,606	59, I	343,570	45, I	213,604	52, I
North							
69	500	2,540,668	71, I	8,064,276	49, I	3,767,278	67, I
94	500	2,791,038	81, I	4,116,082	56, I	5,801,358	41, I
79	500	6,544,252	47, I	> 10,000,000		> 10,000,000	
58	500	> 10,000,000		> 10,000,000		> 10,000,000	
81	600	328,582	32, S	944,152	20, I	150,684	41, I
92	600	434,968	33, S	1,904,194	56, SS	568,282	74, I
56	600	840,764	53, I	1,700,638	76, SS	106,902	36, I
71	600	1,572,070	50, I	2,879,354	36, I	1,307,644	52, I
73	700	167,730	112, S	321,576	23, I	106,318	41, I
87	700	171,618	28, I	260,672	23, I	468,616	34, I
50	700	203,216	31, I	339,696	34, I	150,650	28, S
64	700	431,318	31, I	83,640	36, I	375,512	37, I

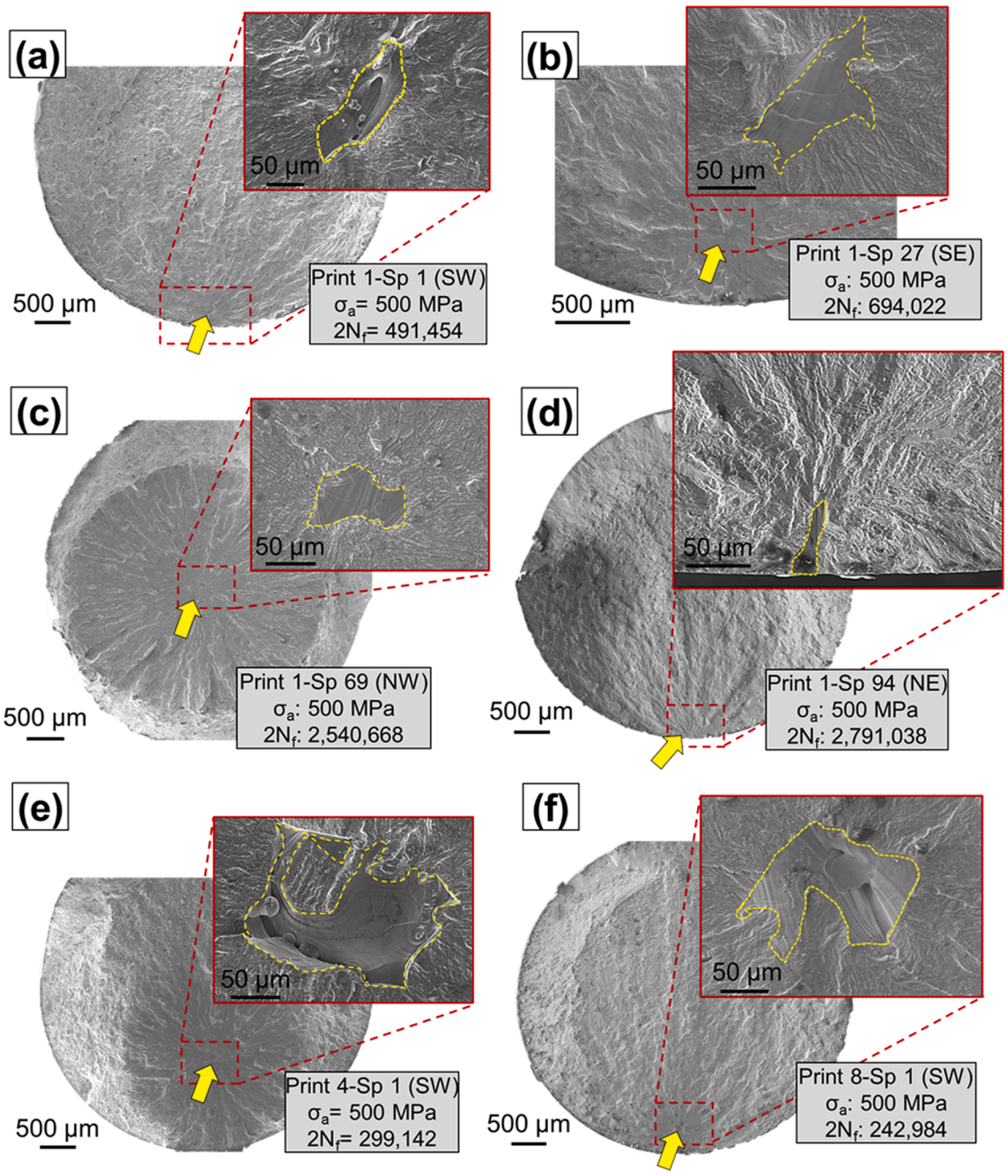

Fig. 14. Fracture surfaces of fatigue specimens including (a) Print 1-Sp1, (b) Print 4-Sp1, (c) Print 8-Sp1, (d) Print 1-Sp27, (e) Print 1-Sp 69, and (f) Print 1-Sp 94. All specimens were tested at 500 MPa stress amplitude. The fatigue life corresponding to each specimen is labeled on each figure. The yellow arrows indicate the crack initiation sites, and the crack-initiating defects are enclosed by yellow dashed lines in the zoomed-in images. (For interpretation of the references to color in this figure legend, the reader is referred to the web version of this article.)

4. Discussion on experimental results

It is well established that the size of critical defects resulting in fatigue failures follows the largest extreme value Gumbel distribution [80]. In this regard, $\sqrt{area}$ of defects were measured based on Murakami's approach [77]. Then, the defects were ranked based on their size from the smallest to the largest one. Lastly, the reduced variate (Y_i) was obtained by:

$$Y_i = -ln(-ln(i/N+1)) \quad (1)$$

where i is the rank and N is the total number of critical defects. The plots of the reduced variates of different prints for both north and south locations are presented in Fig. 15(a) & (b), respectively. As seen in Fig. 15(a), the critical defects in the fatigue specimens well obeyed the largest extreme value Gumbel distribution with R^2 values>0.80 for all conditions. In addition, it was seen that in the north, the smallest critical defects occurred in Print 4 specimens. In the south, however, the largest defect was in Print 8, followed by Print 4, which were both considerably larger than that of Print 1. The cumulative and probability density functions (CDF and PDF) were also evaluated using equations (2) and (3) according to ASTM E2283 [81]:

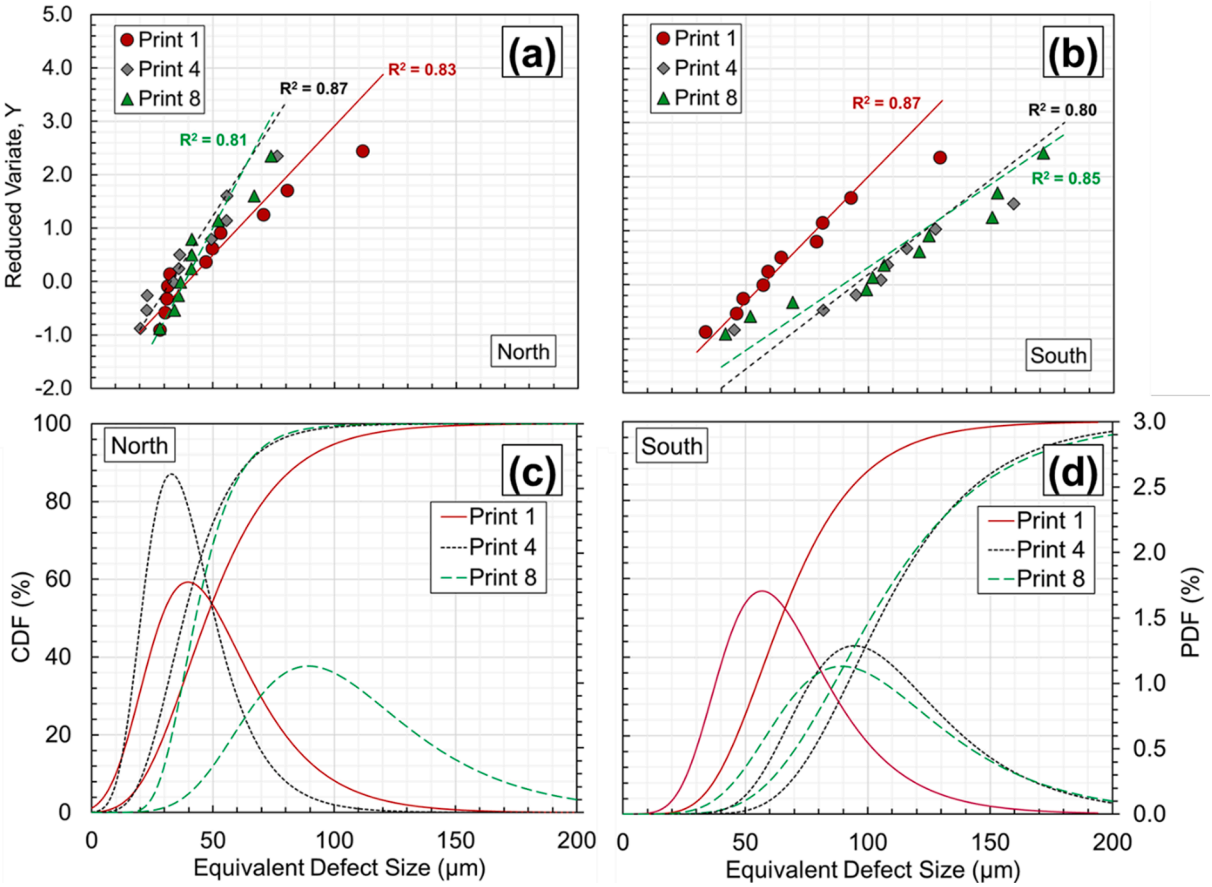

Fig. 15. The extreme value Gumbel distributions of critical defect size for Prints 1, 4, and 8 specimens in the (a) north and (b) south and the corresponding CDF and PDF in the (c) north and (d) south.

Table 5
Location (λ) and scale (δ) parameters of the Gumbel's extreme value distribution.

Gumbel Parameters	Print 1		Print 4		Print 8	
Build Plate Location	North	South	North	South	North	South
Location Parameter, λ	40	57	33	95	39	89
Scale Parameter, δ	21	22	14	29	12	33

$$PDF(x) = 1/\delta\left[exp\left(-\left(\sqrt{area_{defect}}-\lambda\right)/\delta\right)\right] \times exp\left[-exp\left(-\left(\sqrt{area_{defect}}-\lambda\right)/\delta\right)\right] \quad (2)$$

$$CDF(x) = exp\left[-exp\left(-\left(\sqrt{area_{defect}}-\lambda\right)/\delta\right)\right] \quad (3)$$

where the λ and δ are location and scale parameters, respectively, and their values are reported in Table 5 [53,81].

The statistics of fatigue critical defect size, presented in Fig. 15, appeared to be in good agreement with the orders of data presented in Fig. 13 that the difference in fatigue life between north and south was small in Print 1, which became larger in Print 4 and small again in Print 8. In order to better quantify the change in location dependency, the log-normal distributions of fatigue lives for all prints and locations at the stress amplitude of 600 MPa were indicated in Fig. 16. The reused fatigue life improved in the north of Print 4, which was noted in Fig. 12, and clearly evident in Fig. 16. Comparing the PDF curves in Fig. 15(c) & (d), it is evident that the ranges of critical defects in both north and south were essentially identical for Print 1.

This indicates the fabrication with unused powder had very limited

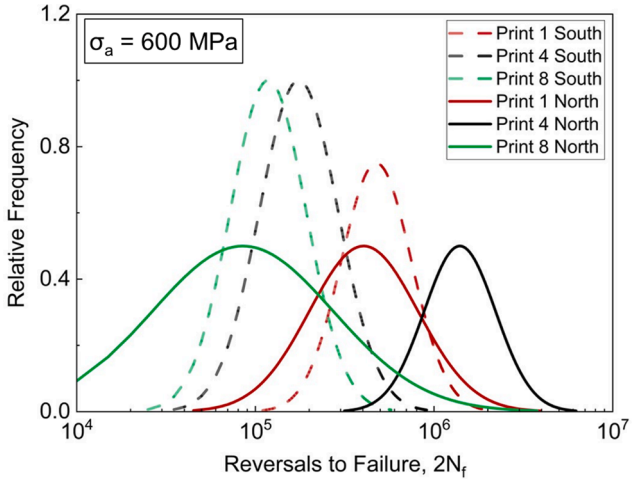

Fig. 16. The log-normal distribution of fatigue lives for Prints 1, 4, and 8 in the north and south at the stress amplitude of 600 MPa.

spatter. As the powder was reused, the O and N pickup in the powder could result in more significant spattering, leading to more and larger defects in the downstream locations. Indeed, the critical defects in the south of Print 4 became significantly larger, while those in the north did not experience much change. Excessive O and N pickup due to further reuse of the powder exacerbated the spattering in both south and north locations. This could be the case for Print 8, where the size ranges of the critical defects in both north and south were similarly large. This

observation on the equivalent diameter of critical defects matched the fatigue behavior.

5. Conclusions

This study investigated the effects of reusing plasma atomized Ti-6Al-4V Grade 5 powder in an L-PBF system on microstructure, porosity, and mechanical properties. In addition, parts were distributed across the build plate to evaluate the effect of location on the part mechanical performance. The following conclusions were drawn based on the experimental results and analysis:

- Powder reuse (up to 7x) increased the powder D-values and uniformity, resulting in higher flowability and packing state.
- Reusing the powder up to 7x did not affect the microstructure. Based on the X-ray computed tomography scans performed on the witness coupons, the defect size and count generally increased in the direction of gas flow, which was attributed to the spattering during fabrication. Limited powder reuse up to 3 times appeared to decrease the defect content; however, it increased again with further reuse.
- The yield and ultimate tensile strength gradually increased with powder reuse up to 7x by ~ 2 % due to higher oxygen concentration in reused powders. In addition, specimens closer to the gas flow outlet (i.e., downstream/south) had higher strength by ~ 1 % due to more heat-affected powders in this zone and, consequently, higher oxygen content. Tensile ductility had an opposite trend, indicating lower ductility for the specimens manufactured from reused powder up to ~ 10 % and/or closer to the gas flow outlet up to ~ 18 %.
- The high strain-rate fracture behavior of specimens from the reused powder showed a higher critical energy release rate (3–4 %) because of the increased yield strength. However, no location dependency effect on the fracture behavior was noticed.
- Although limited powder reuse (up to 3x) could moderately reduce defect content in parts and improve the fatigue performance of the specimens closer to the gas flow inlet, it generally decreased fatigue resistance due to higher oxygen content and spattering when reuse was excessive (up to 7x) and/or fabrication was at downstream locations.
- Results showed that some mechanical properties, including tensile strength and high strain-rate performance, were less sensitive to changes in powder and location in L-PBF Ti64. However, care must be taken for fatigue-critical applications, where defect factors (e.g., size, shape, and location) can play a major role.

The knowledge obtained in this study can provide further insight into different sources of variabilities (i.e., location and powder) of part performance. Controlling or monitoring such variabilities during the L-PBF fabrication can result in more reliable parts or ones with more predictable mechanical properties, which is essential for the qualification and certification of AM parts in load-bearing critical applications [82,83].

Declaration of Competing Interest

The authors declare that they have no known competing financial interests or personal relationships that could have appeared to influence the work reported in this paper.

Data availability

Data will be made available on request.

Acknowledgments

This material is based upon work partially supported by the Federal Aviation Administration under Award No. FAA-12-C-AM-AU-003, and the National Science Foundation (NSF) under Award No. 1919818. The support from Dr. Mahdi Habibnejad from Advanced Powder and Coating (AP&C), a General Electrics (GE) Additive Company, to characterize the powder PSD and chemical composition is greatly appreciated.

Appendix A. Supplementary material

Supplementary data to this article can be found online at https://doi.org/10.1016/j.ijfatigue.2022.107343.

References

[1] Pegues JW, Shao S, Shamsaei N, Sanaei N, Fatemi A, Warner DH, et al. Fatigue of additive manufactured Ti-6Al-4V, Part I: the effects of powder feedstock, manufacturing, and post-process conditions on the resulting microstructure and defects. Int J Fatigue 2020;132. https://doi.org/10.1016/j.ijfatigue.2019.105358.
[2] America Makes & ANSI Additive Manufacturing Standardization Collaborative (AMSC). Standardization roadmap for additive manufacturing - Version 2.0. vol. 2; 2018.
[3] Soundarapandiyan G, Johnston C, Khan RHU, Leung CLA, Lee PD, Hernández-Nava E, et al. The effects of powder reuse on the mechanical response of electron beam additively manufactured Ti6Al4V parts. Addit Manuf 2021;46. https://doi.org/10.1016/j.addma.2021.102101.
[4] Schur R, Ghods S, Wisdom C, Pahuja R, Montelione A, Arola D, et al. Mechanical anisotropy and its evolution with powder reuse in Electron Beam Melting AM of Ti6Al4V. Mater Des 2021;200. https://doi.org/10.1016/j.matdes.2021.109450.
[5] Schur R, Ghods S, Schultz E, Wisdom C, Pahuja R, Montelione A, et al. A fractographic analysis of additively manufactured Ti6Al4V by electron beam melting: effects of powder reuse. J Fail Anal Prev 2020;20:794–803. https://doi.org/10.1007/s11668-020-00875-0.
[6] Tang HP, Qian M, Liu N, Zhang XZ, Yang GY, Wang J. Effect of powder reuse times on additive manufacturing of Ti-6Al-4V by selective electron beam melting. JOM 2015;67:555–63. https://doi.org/10.1007/s11837-015-1300-4.
[7] Popov VV, Katz-Demyanetz A, Garkun A, Bamberger M. The effect of powder recycling on the mechanical properties and microstructure of electron beam melted Ti-6Al-4V specimens. Addit Manuf 2018;22:834–43. https://doi.org/10.1016/j.addma.2018.06.003.
[8] Derimow N, Gorham JM, Martin ML, Benzing JT, White RM, Hrabe N. Surface chemistry in Ti-6Al-4V feedstock as influenced by powder reuse in electron beam additive manufacturing. Appl Surf Sci 2022;602. https://doi.org/10.1016/j.apsusc.2022.154280.
[9] Gruber H, Karimi P, Hryha E, Nyborg L. Effect of powder recycling on the fracture behavior of electron beam melted alloy 718. Powder Metall Prog 2018;18:40–8. https://doi.org/10.1515/pmp-2018-0005.
[10] Guo Y, Chen C, Wang Q, Liu M. Effects of reuse on the properties of tantalum powders and tantalum parts additively manufactured by electron beam powder bed fusion. Mater Res Express 2021:8. https://doi.org/10.1088/2053-1591/abf60e.
[11] Carrion PE, Soltani-Tehrani A, Phan N, Shamsaei N. Powder recycling effects on the tensile and fatigue behavior of additively manufactured Ti-6Al-4V parts. JOM 2019;71:963–73. https://doi.org/10.1007/s11837-018-3248-7.
[12] Alamos FJ, Schiltz J, Kozlovsky K, Attardo R, Tomonto C, Pelletiers T, et al. Effect of powder reuse on mechanical properties of Ti-6Al-4V produced through selective laser melting. Int J Refract Met Hard Mater 2020;91. https://doi.org/10.1016/j.ijrmhm.2020.105273.
[13] Soltani-Tehrani A, Yasin MS, Shao S, Shamsae. Effects of powder reuse and spatial location dependency on the powder characteristics and defect structure of additively manufactured Ti-6Al-4V parts. In: Proc. 32nd Annu. Int. Solid Free. Fabr. Symp. - An Addit. Manuf. Conf.; 2021. p. 1093–103.
[14] Contaldi V, Corrado P, Del Re F, Di Martino D, Di Petta P, Palumbo B, et al. Direct metal laser sintering of Ti-6Al-4V parts with reused powder. Int J Adv Manuf Technol 2022. https://doi.org/10.1007/s00170-022-08807-y.
[15] Skalon M, Meier B, Leitner T, Arneitz S, Amancio-Filho ST, Sommitsch C. Reuse of Ti6al4V powder and its impact on surface tension, melt pool behavior and mechanical properties of additively manufactured components. Materials (Basel) 2021;14:1–22. https://doi.org/10.3390/ma14051251.
[16] Harkin R, Wu H, Nikam S, Yin S, Lupoi R, McKay W, et al. Powder reuse in laser-based powder bed fusion of Ti6Al4V—changes in mechanical properties during a powder top-up regime. Materials (Basel) 2022;15:2238. https://doi.org/10.3390/ma15062238.
[17] Soltani-Tehrani A, Pegues J, Shamsaei N. Fatigue behavior of additively manufactured 17–4 PH stainless steel: the effects of part location and powder reuse. Addit Manuf 2020;36. https://doi.org/10.1016/j.addma.2020.101398.
[18] Jacob G, Brown CU, Donmez A, Watson SS, Donmez MA, Watson SS, et al. Effects of powder recycling on stainless steel powder and built material properties in metal powder bed fusion processes. vol. Series 100. Gaithersburg, MD; 2017. doi: 10.6028/NIST.AMS.100-6.
[19] Ahmed F, Ali U, Sarker D, Marzbanrad E, Choi K, Mahmoodkhani Y, et al. Study of powder recycling and its effect on printed parts during laser powder-bed fusion of 17–4 PH stainless steel. J Mater Process Tech 2019;278. https://doi.org/10.1016/j.jmatprotec.2019.116522.

[20] Sun H, Chu X, Liu Z, Gisele A, Zou Y. Selective laser melting of maraging steels using recycled powders: a comprehensive microstructural and mechanical investigation. Metall Mater Trans A Phys Metall Mater Sci 2021;52:1714–22. https://doi.org/10.1007/s11661-021-06180-1.
[21] Berez J, Saldana C. Fatigue of laser powder bed fusion processed 17–4 stainless steel using prior process exposed powder feedstock. J Manuf Process 2021;71:515–27. https://doi.org/10.1016/j.jmapro.2021.09.045.
[22] Lu C, Zhang R, Xiao M, Wei X, Yin Y, Qu Y, et al. A comprehensive characterization of virgin and recycled 316L powders during laser powder bed fusion. J Mater Res Technol 2022;18:2292–309. https://doi.org/10.1016/j.jmrt.2022.03.125.
[23] Fedina T, Sundqvist J, Kaplan AFH. Spattering and oxidation phenomena during recycling of low alloy steel powder in Laser Powder Bed Fusion. Mater Today Commun 2021;27.
[24] Yi F, Zhou Q, Wang C, Yan Z, Liu B. Effect of powder reuse on powder characteristics and properties of Inconel 718 parts produced by selective laser melting. J Mater Res Technol 2021;13:524–33. https://doi.org/10.1016/j.jmrt.2021.04.091.
[25] Kim S, Goto M, Kim S. Effect of powder recycling on environment-assisted fracture of inconel 718 alloy fabricated by laser powder bed fusion. Metall Mater Trans A Phys Metall Mater Sci 2022;53:211–24. https://doi.org/10.1007/s11661-021-06514-z.
[26] Bhowmik S, Mcwilliams BA, Knezevic M. Materials Characterization Effect of powder reuse on tensile, compressive, and creep strength of Inconel 718 fabricated via laser powder bed fusion. Mater Charact 2022;190. https://doi.org/10.1016/j.matchar.2022.112023.
[27] Soltani-Tehrani A, Shamsaei N, Surya AV, Mallory J, Ramakrishnan R. Powder reuse effects on the tensile behavior of additively manufactured inconel 718 parts. In: Solid Free. Fabr. 2021 Proc. 32nd Annu. Int. Solid Free. Fabr. Symp. - An Addit. Manuf. Conf.; 2021. p. 948–57.
[28] Del Re F, Contaldi V, Astarita A, Palumbo B, Squillace A, Corrado P, et al. Statistical approach for assessing the effect of powder reuse on the final quality of AlSi10Mg parts produced by laser powder bed fusion additive manufacturing. Int J Adv Manuf Technol 2018;97:2231–40. https://doi.org/10.1007/s00170-018-2090-y.
[29] Weiss C, Haefner CL, Munk J. On the influence of AlSi10Mg powder recycling behavior in the LPBF process and consequences for mechanical properties. Jom 2022. https://doi.org/10.1007/s11837-021-05080-4.
[30] Carroll JD, Exil AN, DeJong SA, Valdez IA, Laursen CM, Deibler LA, et al. High-throughput statistical interrogation of mechanical properties with build plate location and powder reuse in AlSi10Mg. JOM 2021;73:3356–70. https://doi.org/10.1007/s11837-021-04888-4.
[31] He X, Kong D, Zhou Y, Wang L, Ni X, Zhang L, et al. Powder recycling effects on porosity development and mechanical properties of Hastelloy X alloy during laser powder bed fusion process. Addit Manuf 2022;55. https://doi.org/10.1016/j.addma.2022.102840.
[32] Yadollahi A, Shamsaei N. Additive manufacturing of fatigue resistant materials: challenges and opportunities. Int J Fatigue 2017;98:14–31. https://doi.org/10.1016/j.ijfatigue.2017.01.001.
[33] Mussatto A, Groarke R, Vijayaraghavan RK, Hughes C, Obeidi MA, Doğu MN, et al. Assessing dependency of part properties on the printing location in laser-powder bed fusion metal additive manufacturing. Mater Today Commun 2022;30. https://doi.org/10.1016/j.mtcomm.2022.103209.
[34] Leung CLA, Marussi S, Towrie M, Atwood RC, Withers PJ, Lee PD. The effect of powder oxidation on defect formation in laser additive manufacturing. Acta Mater 2019;166:294–305. https://doi.org/10.1016/j.actamat.2018.12.027.
[35] Esmaeilizadeh R, Ali U, Keshavarzkermani A, Mahmoodkhani Y, Marzbanrad E, Toyserkani E. On the effect of spatter particles distribution on the quality of Hastelloy X parts made by laser powder-bed fusion additive manufacturing. J Manuf Process 2019;37:11–20. https://doi.org/10.1016/j.jmapro.2018.11.012.
[36] Montalbano T, Briggs BN, Waterman JL, Nimer S, Peitsch C, Sopcisak J, et al. Uncovering the coupled impact of defect morphology and microstructure on the tensile behavior of Ti-6Al-4V fabricated via laser powder bed fusion. J Mater Process Technol 2021;294. https://doi.org/10.1016/j.jmatprotec.2021.117113.
[37] Cain V, Thijs L, Van Humbeeck J, Van Hooreweder B, Knutsen R. Crack propagation and fracture toughness of Ti6Al4V alloy produced by selective laser melting. Addit Manuf 2015;5:68–76. https://doi.org/10.1016/j.addma.2014.12.006.
[38] Mohammadhosseini A, Masood SH, Fraser D, Jahedi M. Dynamic compressive behaviour of Ti-6Al-4V alloy processed by electron beam melting under high strain rate loading. Adv Manuf 2015;3:232–43. https://doi.org/10.1007/s40436-015-0119-0.
[39] Rodriguez OL, Allison PG, Whittington WR, El Kadiri H, Rivera OG, Barkey ME. Strain rate effect on the tension and compression stress-state asymmetry for electron beam additive manufactured Ti6Al4V. Mater Sci Eng A 2018;713:125–33. https://doi.org/10.1016/j.msea.2017.12.062.
[40] Isaac JP, Lee S, Shamsaei N, Tippur HV. Dynamic fracture behavior of additively manufactured Scalmalloy®: Effects of build orientation, heat-treatment and loading-rate. Mater Sci Eng A 2021;826. https://doi.org/10.1016/j.msea.2021.141978.
[41] ASTM International. F2924-14 Standard Specification for Additive Manufacturing Titanium-6 Aluminum-4 Vanadium with Powder Bed Fusion. West Conshohocken, PA; ASTM Int 2014. doi: 10.1520/F2924-14.2.
[42] Santecchia E, Spigarelli S, Cabibbo M. Material reuse in laser powder bed fusion: Side effects of the laser—metal powder interaction. Metals (Basel) 2020;10:1–21. https://doi.org/10.3390/met10030341.
[43] Moghimian P, Poirié T, Habibnejad-Korayem M, Zavala JA, Kroeger J, Marion F, et al. Metal powders in additive manufacturing: a review on reusability and recyclability of common titanium, nickel and aluminum alloys. Addit Manuf 2021:. https://doi.org/10.1016/j.addma.2021.102017.
[44] ASTM International. E466 Standard Practice for Conducting Force Controlled Constant Amplitude Axial Fatigue Tests of Metallic Materials. West Conshohocken, PA; ASTM Int 2015. doi: 10.1520/E0466-15.2.
[45] ASTM International. E8/E8M Standard Test Methods for Tension Testing of Metallic Materials. West Conshohocken, PA; ASTM Int 2016. doi: 10.1520/E0008_E0008M-13.
[46] Isaac JP, Dondeti S, Tippur HV. Fracture behavior of additively printed ABS: effects of print architecture and loading rate. Int J Solids Struct 2021;212:80–95. https://doi.org/10.1016/j.ijsolstr.2020.11.027.
[47] Schindelin J, Arganda-Carreras I, Frise E, Kaynig V, Longair M, Pietzsch T, et al. Fiji: an open-source platform for biological-image analysis. Nat Methods 2012;9:676–82. https://doi.org/10.1038/nmeth.2019.
[48] ASTM International. B215 Standard Practices for Sampling Metal Powders. West Conshohocken, PA; ASTM Int 2020. doi: 10.1520/B0215-15.
[49] ASTM International. E1409-13 Standard Test Method for Determination of Oxygen and Nitrogen in Titanium and Titanium Alloys by Inert Gas Fusion. West Conshohocken, PA; ASTM Int 2016. doi: 10.1520/E1409-13.2.
[50] ASTM International. D7891 Standard Test Method for Shear Testing of Powders Using the Freeman Technology FT4 Powder Rheometer Shear Cell. West Conshohocken, PA; ASTM Int 2015. doi: 10.1520/D7891-15.
[51] Freeman Technology. FT4 Powder Rheometer - Summary of Methodologies 2008.
[52] Tan JH, Wong WLE, Dalgarno KW. An overview of powder granulometry on feedstock and part performance in the selective laser melting process. Addit Manuf 2017;18:228–55. doi: 10.1016/j.addma.2017.10.011.
[53] Soltani-Tehrani A, Habibnejad-Korayem M, Shao S, Haghshenas M, Shamsaei N. Ti-6Al-4V powder characteristics in laser powder bed fusion: the effect on tensile and fatigue behavior. Addit Manuf 2021;51. https://doi.org/10.1016/j.addma.2021.102584.
[54] Emminghaus N, Bernhard R, Hermsdorf J, Kaierle S. Residual oxygen content and powder recycling: effects on microstructure and mechanical properties of additively manufactured Ti-6Al-4V parts. Int J Adv Manuf Technol 2022;121:3685–701.
[55] Brika SE, Letenneur M, Dion CA, Brailovski V. Influence of particle morphology and size distribution on the powder flowability and laser powder bed fusion manufacturability of Ti-6Al-4V alloy. Addit Manuf 2020;31. https://doi.org/10.1016/j.addma.2019.100929.
[56] Sutton AT, Kriewall CS, Leu MC, Newkirk JW, Brown B. Characterization of laser spatter and condensate generated during the selective laser melting of 304L stainless steel powder. Addit Manuf 2020;31. https://doi.org/10.1016/j.addma.2019.100904.
[57] Sutton AT, Kriewall CS, Karnati S, Leu MC, Newkirk JW. Characterization of AISI 304L stainless steel powder recycled in the laser powder-bed fusion process. Addit Manuf 2020;32. https://doi.org/10.1016/j.addma.2019.100981.
[58] Seyda V, Kaufmann N, Emmelmann C. Investigation of aging processes of Ti-6Al-4V powder material in laser melting. Phys Procedia 2012;39:425–31. https://doi.org/10.1016/j.phpro.2012.10.057.
[59] Pauzon C, Raza A, Hryha E, Forêt P. Oxygen balance during laser powder bed fusion of Alloy 718. Mater Des 2021;201. https://doi.org/10.1016/j.matdes.2021.109511.
[60] Williams R, Bilton M, Harrison N, Fox P. The impact of oxidised powder particles on the microstructure and mechanical properties of Ti-6Al-4 V processed by laser powder bed fusion. Addit Manuf 2021;46. https://doi.org/10.1016/j.addma.2021.102181.
[61] Habibnejad-korayem M, Zhang J, Zou Y. Effect of particle size distribution on the flowability of plasma atomized Ti-6Al-4V powders. Powder Technol 2021;392:536–43. https://doi.org/10.1016/j.powtec.2021.07.026.
[62] Renishaw plc. Investigating the effects of multiple re-use of Ti6Al4V powder in additive manufacturing. 2016.
[63] Cordova L, Campos M, Tinga T. Revealing the effects of powder reuse for selective laser melting by powder characterization. JOM 2019;71:1062–72. https://doi.org/10.1007/s11837-018-3305-2.
[64] Pauzon C, Dietrich K, Forêt P, Dubiez-Le Goff S, Hryha E, Witt G. Control of residual oxygen of the process atmosphere during laser-powder bed fusion processing of Ti-6Al-4V. Addit Manuf 2021;38. https://doi.org/10.1016/j.addma.2020.101765.
[65] Lütjering G, Williams JC. Titanium matrix composites. Springer; 2007.
[66] Pauzon C, Forêt P, Hryha E, Arunprasad T, Nyborg L. Argon-helium mixtures as Laser-Powder Bed Fusion atmospheres: towards increased build rate of Ti-6Al-4V. J Mater Process Technol 2020;279. https://doi.org/10.1016/j.jmatprotec.2019.116555.
[67] Khorasani M, Ghasemi AH, Awan US, Hadavi E, Leary M, Brandt M, et al. A study on surface morphology and tension in laser powder bed fusion of Ti-6Al-4V. Int J Adv Manuf Technol 2020;111:2891–909. https://doi.org/10.1007/s00170-020-06221-w.
[68] Emminghaus N, Hoff C, Hermsdorf J, Kaierle S. Residual oxygen content and powder recycling: effects on surface roughness and porosity of additively manufactured Ti-6Al-4V. Addit Manuf 2021:46. https://doi.org/10.1016/j.addma.2021.102093.
[69] Sanaei N, Fatemi A. Analysis of the effect of surface roughness on fatigue performance of powder bed fusion additive manufactured metals. Theor Appl Fract Mech 2020;108.
[70] Pegues J, Roach M, Scott Williamson R, Shamsaei N. Surface roughness effects on the fatigue strength of additively manufactured Ti-6Al-4V. Int J Fatigue 2018;116:543–52. https://doi.org/10.1016/j.ijfatigue.2018.07.013.

[71] Caracciolo P. Effect of Defect in Additive Manufacturing Products. In: Int. Conf. Addit. Manuf. 3D Print., Nottingham (UK); 2018.
[72] Collins CR, Dear FF, Rugg D, Dye D. The effect of dissolved nitrogen on the fatigue behavior of Ti-6Al-4V. Metall Mater Trans A 2021;52:1596–608.
[73] Derimow N, Hrabe N. Oxidation in reused powder bed fusion additive manufacturing Ti-6Al-4V feedstock: a brief review. Jom 2021;73:3618–38. https://doi.org/10.1007/s11837-021-04872-y.
[74] Wasz ML, Brotzen FR, McLellan RB, Griffin AJ. Effect of oxygen and hydrogen on mechanical properties of commercial purity titanium. Int Mater Rev 1996;41:1–12. https://doi.org/10.1179/imr.1996.41.1.1.
[75] Dietrich K, Diller J, Dubiez-Le Goff S, Bauer D, Forêt P, Witt G. The influence of oxygen on the chemical composition and mechanical properties of Ti-6Al-4V during laser powder bed fusion (L-PBF). Addit Manuf 2020;32. https://doi.org/10.1016/j.addma.2019.100980.
[76] Yang KV, de Looze GR, Nguyen V, Wilson RS. Directed-energy deposition of Ti-6Al-4V alloy using fresh and recycled feedstock powders under reactive atmosphere. Addit Manuf 2022;58. https://doi.org/10.1016/j.addma.2022.103043.
[77] Murakami Y, Endo M. Effects of defects, inclusions and inhomogeneities on fatigue strength. Int J Fatigue 1994;16:163–82. https://doi.org/10.1016/0142-1123(94)90001-9.
[78] Fernandez A, Pautler SE. Metal fatigue causing cystoscope rupture during bladder neck incision. JSLS J Soc Laparoendosc Surg 2011;15:421–3. https://doi.org/10.4293/108680811X13125733356710.
[79] Soltani-Tehrani A, Shrestha R, Phan N, Seifi M, Shamsaei N. Establishing specimen property to part performance relationships for laser beam powder bed fusion additive manufacturing. Int J Fatigue 2021;151. https://doi.org/10.1016/j.ijfatigue.2021.106384.
[80] Beretta S, Anderson C, Murakami Y. Extreme value models for the assessment of steels containing multiple types of inclusion. Acta Mater 2006;54:2277–89. https://doi.org/10.1016/j.actamat.2006.01.016.
[81] ASTM International. E2283 Standard Practice for Extreme Value Analysis of Nonmetallic Inclusions in Steel and Other Microstructural Features. West Conshohocken, PA; ASTM Int 2019. doi: 10.1520/E2283-08R19.1.
[82] Seifi M, Gorelik M, Waller J, Hrabe N, Shamsaei N, Daniewicz S, et al. Progress towards metal additive manufacturing standardization to support qualification and certification. Jom 2017;69:439–55. https://doi.org/10.1007/s11837-017-2265-2.
[83] Russell R, Wells D, Waller J, Poorganji B, Ott E, Nakagawa T, et al. Qualification and certification of metal additive manufactured hardware for aerospace applications. Addit Manuf Aerosp Ind 2019. https://doi.org/10.1016/b978-0-12-814062-8.00003-0.